A 1.5MHz Time-Based Boost Converter with Feedback-PID for AMOLED Displays with Delay-Line-Based Line Feedforward

Paolo Melillo(1), Mauro Leoncini(1), Gabriele Magni(1), Alessandro Bertolini(2), Alessandro Gasparini(2), Massimo Ghioni(1)
Email: mauro.leoncini@polimi.it
(1) Politecnico di Milano, DEIB, Milan, Italy
(2) STMicroelectronics, AMS R&D, Milan

***Abstract*—In recent years, time-based compensators have been investigated as a promising alternative to conventional analog control schemes for high-frequency DC-DC converters. As the voltage-mode time-based implementation lacks a PWM ramp generator, implementing a line feedforward is not straightforward. To solve this problem, a different type of compensator, referred to as feedback-PID (F-PID), has been used in this work. This compensator is composed of a proportional-integral forward path and a band-pass-filter feedback path, which can be easily modified to include the feedforward injection from the input voltage. In this paper, the proposed F-PID compensator is presented, and its implementation in a time-based compensator with delay-line-based line-feedforward is discussed. To verify the analysis, a prototype boost converter for AMOLED displays with a 1.5MHz switching frequency is realized in a 180nm BCD process. Measurement results show a 40mV peak-to-peak variation when an input voltage variation of 1V in 50μs is applied, and a duty-cycle RMS jitter of 1.5ns. The proposed controller occupies only 0.23mm^2.**

***Index Terms*—Boost converter, time-based control, feedback-PID, feed-forward, fast response, line transient.**

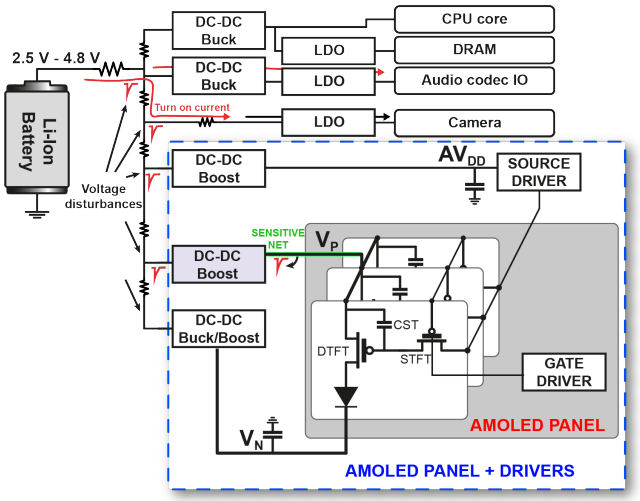

Fig. 1. Block diagram of the power management architecture for a portable device with AMOLED panel subsystem.

I. Introduction

BOOST converters are widely used in active matrix organic light emitting diode (AMOLED) displays to generate the positive bias voltage to the thin film transistor (TFT) in the AMOLED panel [1]. Referring to Fig. 1, the source of the TFT is powered by the boost converter; thus, any variations in the converter's output would cause the screen to flicker [2]. In portable devices, abrupt current demands from other loads generate substantial voltage disturbances on the power distribution bus (flat cable). These disturbances propagate to the boost converter's input, potentially causing screen flickering. As is well known in boost converter design, the presence of a right-half-plane (RHP) zero inherently limits the achievable control bandwidth, making it challenging to achieve fast line transient response [3]. Consequently, line feedforward becomes mandatory in this scenario to ensure adequate disturbance rejection. Moreover, area occupation and power consumption in portable devices are constrained by the available space on the devices and the battery life-time, respectively. In such applications, implementing the compensator with a time-based approach would help reduce the silicon area and the power consumption required by the control loop [4], [5], [6], [7], [8]. A time-based compensator, shown in Fig. 2, is composed of two main elements, a voltage-controlled oscillator (VCO) and a voltage-controlled delay line (VCDL) with differential outputs. The VCO is responsible for the integration in the phase domain, while the VCDL adds a time delay (phase shift) proportional to its inputs. The VCO sub-block is composed of a transconductor $G_{m\mathrm{I}}$ and two current-controlled oscillators (CCOs). The VCDL sub-block is composed of two transconductors, $G_{m\mathrm{P}}$ and $G_{m\mathrm{D}}$, for the proportional and the derivative gain, respectively, and two current-controlled delay lines (CCDLs). Although the derivative function can be implemented in the time domain [9], a straightforward workaround is to make the derivative in the voltage domain by employing a simple high-pass filter ($C_{\mathrm{D}}R_{\mathrm{D}}$). The PWM signal is then generated via a simple digital circuit, the phase detector (PD), which detects the time difference between the square-wave signals at its inputs. The PD shows a fixed gain that cannot be modulated, preventing the application of conventional feedforward techniques [10]. A specific feedforward scheme

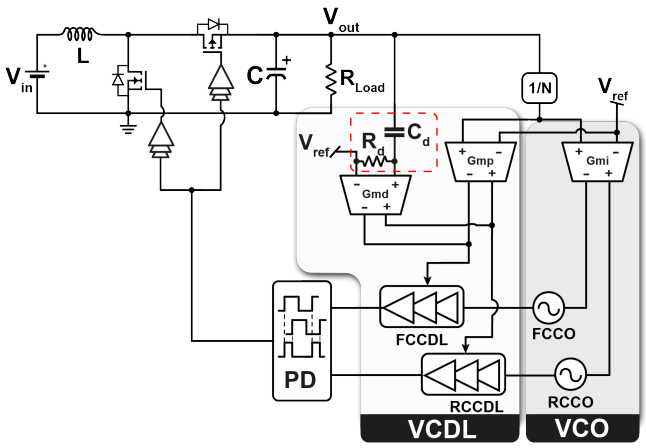

Fig. 2. Time-based boost converter.

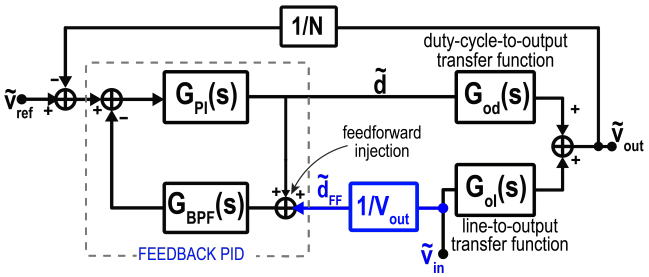

Fig. 3. Small signal model of the boost converter employing the proposed F-PID.

for time-based control is introduced in [7] to solve this issue. Although effective, the reported feedforward scheme requires a wide-range linear differential delay line, which introduces a considerable delay in the loop and occupies a significant amount of area. To overcome these drawbacks, an alternative time-based compensator, referred to as feedback-PID (F-PID), has been used in this paper. The proposed F-PID exploits an additional path to introduce a feedforward without modulating the PD. Basically, the F-PID additional path can be used to modify the converter's duty-cycle, as it generates an additional transfer function, with unity gain, from the injection node to the PD inputs.

This paper is organized as follows. In Sect. II the proposed F-PID is introduced and the analytical expression of the relevant transfer function are provided; in Sect. III the circuit implementation and the behavior are described; measurement results of the boost converter employing the proposed control method are shown in Sect. IV, then, conclusions are drawn in Sect. V.

II. Feedback-PID Compensator

The small-signal model of a boost converter employing feedback-PID is shown in Fig. 3. The F-PID is composed of a forward path, $G_{\mathrm{PI}}(s)$, and a feedback path, $G_{\mathrm{BPF}}(s)$, that can be used as an injection point for the input voltage signal ($\tilde{v}_{in}$). In the forward path, a proportional–integral (PI) compensator

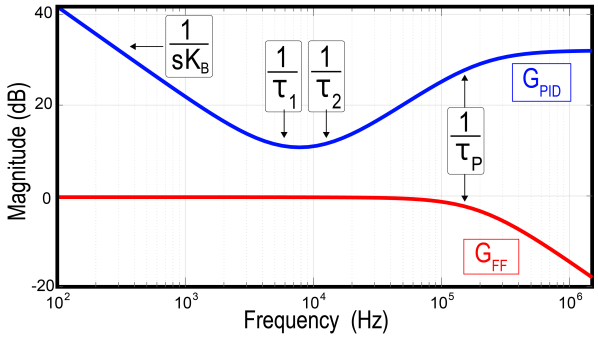

Fig. 4. Bode diagram of the magnitude of the F-PID transfer functions $G_{\text{F-PID}}$ (blue) and G_{FF} (red).

is employed, with transfer function

$$G_{\mathrm{PI}}(s) = \frac{K_{\mathrm{I}}}{s}\left(1+\frac{s}{\omega_{\mathrm{PI}}}\right), \tag{1}$$

with K_{I} being the gain and ω_{PI} being the radiant frequency of the high frequency pole. The feedback block is a band-pass filter (BPF) with transfer function

$$G_{\mathrm{BPF}}(s) = \frac{sK_{\mathrm{B}}}{\left(1+\frac{s}{\omega_1}\right)\left(1+\frac{s}{\omega_2}\right)} \tag{2}$$

with gain $K_{\mathrm{B}} = K_0/\omega_1$ and two poles at ω_1 and ω_2. For this implementation, assuming $K_{\mathrm{I}} \cdot K_{\mathrm{B}} \gg 1$, the structure is equivalent to a PID with transfer function $G_{\text{F-PID}}$ equal to:

$$G_{\text{F-PID}}(s) = \frac{G_{\mathrm{PI}}(s)}{1+G_{\mathrm{PI}}(s)G_{\mathrm{BPF}}(s)} \simeq \frac{\left(1+\frac{s}{\omega_1}\right)\left(1+\frac{s}{\omega_2}\right)}{s\cdot K_{\mathrm{B}}\left(1+\frac{s}{\omega_{\mathrm{P}}}\right)}, \tag{3}$$

where a pole-zero cancellation occurs through the interaction between the BPF and the PI. The F-PID also shows a high frequency pole at angular frequency, ω_{P}:

$$\omega_{\mathrm{P}} = \frac{K_{\mathrm{I}}K_{\mathrm{B}}\cdot\omega_1\omega_2}{\omega_{\mathrm{PI}}}, \tag{4}$$

and its Bode diagram is shown in Fig. 4.

The feedforward signal $\tilde{d}_{\mathrm{FF}} = -\tilde{v}_{in}/V_{out}$, induced by an input voltage variation $\tilde{\mathrm{v}}_{\mathrm{in}}$, is injected at the BPF input. The transfer function from the feedforward injection point to the PD output, $G_{\mathrm{FF}}(s) = \tilde{d}/\tilde{\mathrm{v}}_{in}$, is

$$G_{\mathrm{FF}}(s) = -\frac{G_{\mathrm{BPF}}(s)\cdot G_{\mathrm{PI}}(s)}{1+G_{\mathrm{PI}}(s)\cdot G_{\mathrm{BPF}}(s)} \tag{5}$$

which shows a unity gain at low frequency and a high frequency pole at ω_{P}, as shown in Fig. 4. Referring to the state-space averaged model of the boost converter [3], the *duty-cycle-to-output* and the *line-to-output* transfer functions, G_{od} and G_{ol}, respectively, can be written as:

$$G_{od}(s) = G_{od}(0)\cdot\frac{\left(1-\frac{s}{\omega_{z,rhp}}\right)\left(1+\frac{s}{\omega_{z,lhp}}\right)}{\left(\frac{s^2}{\omega_0^2}+\frac{2s\zeta}{\omega_0}+1\right)} \tag{6}$$

and

$$G_{ol}(s) = \frac{1}{D'}\frac{RD'^2}{(RD'^2+r)}\cdot\frac{\left(1+\frac{s}{\omega_{z,lhp}}\right)}{\left(\frac{s^2}{\omega_0^2}+\frac{2s\zeta}{\omega_0}+1\right)}, \tag{7}$$

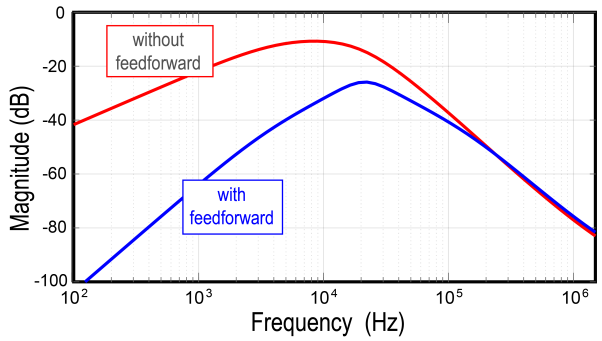

Fig. 5. Closed loop line-to-output transfer function of the boost converter with F-PID controller with (blue) and without (red) the line-feedforward.

where

$$G_{od}(0) = \frac{V_{out}}{D'} \cdot \frac{(RD'^2 - r)}{(RD'^2 + r)}; \tag{8a}$$

$$D' = 1 - D = \frac{V_{in}}{V_{out}} \cdot \eta\,; \tag{8b}$$

$$\omega_0 = \frac{1}{\sqrt{LC}} \cdot \sqrt{\frac{RD'^2 + r}{R}}; \tag{8c}$$

$$Q = \frac{\sqrt{LC \cdot (R + r_C) \cdot (RD'^2 + r)}}{C(r(R + r_C) + RD'^2 r_C) + L}; \tag{8d}$$

$$\omega_{z,lhp} = \frac{1}{C \cdot r_C}; \tag{8e}$$

$$\omega_{z,rhp} = \frac{(RD'^2 - r)}{L}. \tag{8f}$$

In the above equations, R is the load resistance, D the converter's duty-cycle of the converter, ω_0 and Q denote LC filter angular frequency and quality factor respectively, r_C is the series resistance of the output capacitor, and η is the conversion efficiency. The term $r = r_L + R_{on,LS} \cdot D + R_{on,HS} \cdot (1 - D)$ represents the equivalent average resistance (EAR) [11] which accounts the parasitic resistances of the inductor, r_L and of the high-side and low-side power MOSFETs, $R_{on,HS}$ and $R_{on,LS}$, respectively. By employing the F-PID, the closed-loop *line-to-output* transfer function, $G_{ol,FF\text{-}CL}$, becomes:

$$G_{ol,FF\text{-}CL}(s) = \frac{G_{ol}(s) - G_{od}(s)/V_{out} G_{FF}}{1 + G_{LOOP}(s)}, \tag{9}$$

where $G_{LOOP}(s) = G_{F\text{-}PID}(s) G_{od}(s)/N$, being $1/N$ the resistive divider ratio at the converter's output. With the adoption of the F-PID structure, the input voltage information can be directly injected into the compensator network at the BPF input, obtaining a wide bandwidth feedforward action. The simulated closed-loop line-to-output transfer function, $G_{ol,FF\text{-}CL}(s)$, is shown in Fig. 5, also compared with the closed-loop *line-to-output* obtained without the proposed feedforward. The Bode diagrams of the two transfer functions are shown in blue and red, respectively. The comparison shows that the audiosusceptibility of the system adopting line-feedforward is lower over the entire frequency range up to the pole frequency ω_p.

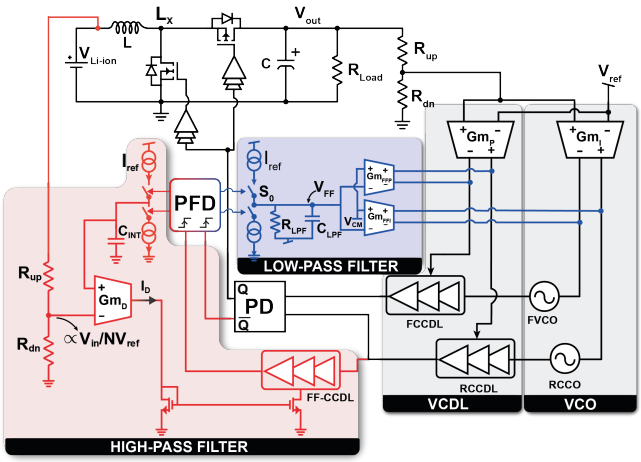

Fig. 6. Simplified circuit diagram of the proposed time-based F-PID controller with delay-line based line-feedforward.

III. Circuit Implementation

The circuit diagram of the F-PID is shown in Fig. 6. The forward path implements a time-based PI controller through the cascade of integral and proportional stages. The integral stage is realized by injecting current from the integral transconductor into two current-controlled oscillators (CCOs), while the proportional stage uses the proportional transconductor to drive two current-controlled delay lines (CCDLs), leading to a transfer function $G_{T\text{-}PI}$, that is,

$$G_{T\text{-}PI}(s) = \frac{G_{mI} \cdot K_{CCO}}{s} + G_{mP} \cdot K_{CCDL}, \tag{10}$$

where G_{mI} and G_{mP} are the integral and proportional transconductors' gains, respectively, and K_{CCO} and K_{CCDL} are the CCO and CCDL gains, respectively.

The feedback path implements a band-pass filter, split into a high-pass and a low-pass filter. The low-pass filter, R_{LPF}, C_{LPF}, receives as input the charge-pump current and, by means of the transconductors G_{mFFI} and G_{mFFP}, injects currents into the CCOs and CCDLs. The high-pass filter (HPF) is realized as an integrator in feedback and is composed of the transconductor G_{mD}, an additional CCDL, denoted as feedforward CCDL (FF-CCDL), a phase and frequency detector (PFD), a charge-pump (CP), and an integrator capacitance C_{INT}. The capacitance voltage is connected to the positive node of the transconductor G_{mD}, thereby closing the feedback loop. The HPF transfer function, $G_{HPF} = \tilde{i}_{int}/\tilde{d}$, i.e., the gain from the duty-ratio, $\tilde{d}$, to the current over the integral capacitor, $\tilde{i}_{int}$, can be written as:

$$G_{HPF}(s) = \frac{s \cdot G_{mD} K_{FF\text{-}CCDL} G_{PFD}/C_{INT}}{1 + s \cdot G_{mD} K_{FF\text{-}CCDL} G_{PFD}/C_{INT}} \cdot I_{ref}, \tag{11}$$

where G_{mD} is the transconductor gain, $K_{FF\text{-}CCDL}$ is the gain of the feedforward CCDL, G_{PFD} and I_{ref} are the PFD gain and the charge-pump current respectively. The charge-pump output is replicated at the input of the low-pass filter (LPF), so that the overall BPF transfer function G_{BPF} is:

$$G_{BPF}(s) = \frac{s \cdot G_{mD} K_{FF\text{-}CCDL} G_{PFD}/C_{INT}}{1 + s \cdot G_{mD} K_{FF\text{-}CCDL} G_{PFD}/C_{INT}} \cdot \frac{I_{ref} \cdot R_{LPF}}{1 + sC_{LPF}R_{LPF}}. \tag{12}$$

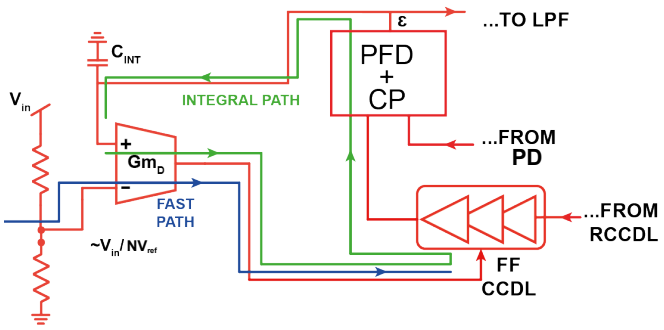

(a)

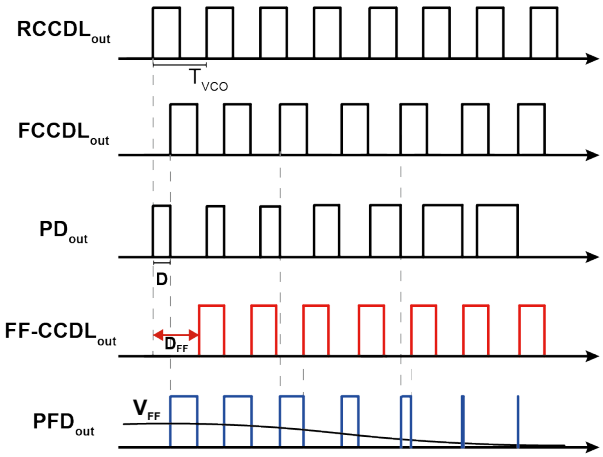

(b)

Fig. 7. High-pass filter implementation (a), timing diagram of signals involved after a sudden variation of the input voltage (b).

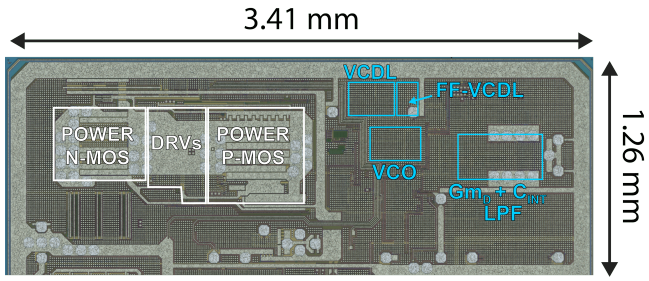

Fig. 8. Die micrograph of the time-based boost converter.

As shown in Fig. 7(a) and Fig. 7(b), a phase-frequency detector (PFD) and a CP are used to make a subtraction between two time signals: the falling edge of the PD output, which sets the beginning of the *off-time*, and the rising edge of the output of the FF-CCDL. This time shift represents the difference between the duty-cycle asserted by the control loop and the feedforward duty-cycle. This difference is zero at steady state, but becomes significant after an abrupt change in input voltage. In this condition, a differential signal is injected into the loop, thereby fastening the actual duty-cycle variation. At steady-state, the small error between the feedforward duty-cycle injected through the *fast path* (Fig. 7(a)), and the actual steady-state duty-cycle is nulled by the *integral path* (Fig.7(b)) and no current is injected in the low-pass filter as shown in the timing diagram in Fig. 7(b). During an input voltage variation,

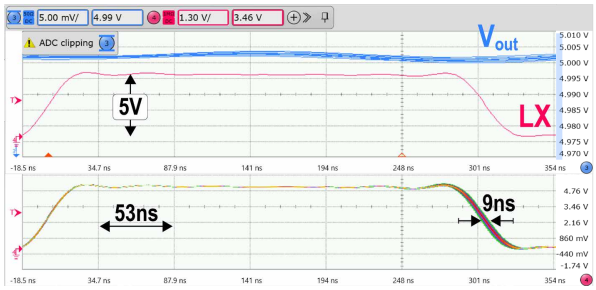

Fig. 9. Measured switching node waveform: single acquisition on the top, and multiple acquisition (i.e., acquisition persistency enabled to evaluate jitter).

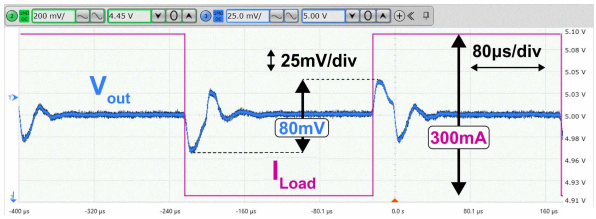

Fig. 10. Measured load transient response to a 300 mA step-like load current variation.

the transconductor, G_{mD}, injects a current in the FF-CCDL, which produces a phase shift with respect to the RCCDL, whose rising edge starts the switching period. The phase shift introduced by the FF-CCDL would match that of the FCCDL at steady state. Contrary to [7], there is no additional delay in the fast signal path (i.e., the proportional action), leading to a higher loop gain's phase margin. Moreover, since the FF-CCDL is a replica of the FCCDL, the delay-line nonlinearities affect both PFD inputs equally, without affecting its output.

IV. Measurement Results

To verify the proposed controller, a prototype boost converter for AMOLED application has been realized in a 180-nm BCD technology. The micrograph is shown in Fig. 8. The die area is 4.09 mm^2 while the controller occupies only 0.23 mm^2. The converter switching frequency is f_{sw} = 1.5 MHz, operating over an input voltage range, V_{in} of 2.5 V to 4.8 V, compatible with standard Li-Ion batteries. The output voltage, V_{out}, is set to 5V while the maximum load current is I_{load} = 600 mA. The output filter consists of an inductor of 2.2 μH and a MLCC output capacitor of 44 μF (14 μF considering de-rating). Fig. 9, top, shows the measured steady-state output voltage and phase node (LX) over a single cycle, highlighting an output voltage ripple of 2.5 mV. In the bottom windows, the superposition of multiple waveforms shows the duty-cycle jitter, with a peak-to-peak value of 9 ns and an RMS of 1.5 ns, equal to 0.2% of the switching period. Figure 10 illustrates the converter response to a load step variation of 300 mA. The peak-to-peak output voltage variation is 80 mV. Figure 11 shows the line transient response of the proposed boost converter when the input voltage varies from 2.7-to-3.7V in 50 μs, and the load current is 300 mA. The peak-to-peak output voltage variation is only 40 mV, demonstrating the effectiveness of the line transient feedforward. Fig. 12

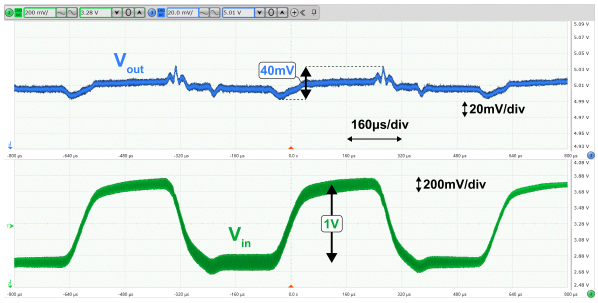

Fig. 11. Measured line transient response to a 1 V input voltage variation in 50 μs (I_{LOAD}=300 mA).

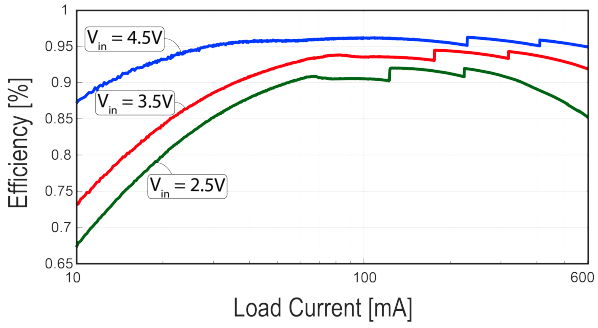

Fig. 12. Measured efficiency of the boost converter at different input voltages. The peak efficiency is 96.1%

shows the efficiency vs. load current of the boost converter at different values of V_{in}. The converter shows a peak of 96.1% and, overall, higher than 80% for all input voltages and across a wide load range (20 to 600 mA). Finally, Table I compares the proposed converter with other boost converters reported in the literature and commercially available products for the AMOLED application. The proposed structure provides similar load and efficiency performance while offering superior line transient responses, comparable to those of the boost converter in [12], which also inherently incorporates line transient improvement through current-mode control. The proposed boost converter achieves these performances with a 30% reduction in the controller area occupation.

V. Conclusions

In this paper, a time-based boost converter with feedback-PID has been presented. The prototype, realized in a 180nm BCD technology operates at 1.5 MHz switching frequency, 2.5-to-4.8 V input voltage, and delivers up to 600 mA load current. The die active area is 4.09 mm^2, while the controller area is only 0.23 mm^2, about 30% less area than that of state-of-the-art controllers. When subject to a 1 V input voltage variation in 50 μs, it shows a peak-to-peak variation of only 40 mV. The load transient response shows an 80 mV peak-to-peak variation, and about 60 μs recovery time. Moreover, the proposed implementation of the HPF in the F-PID feedback path gives an intrinsic low duty-cycle jitter of 1.5 ns, equal to only 0.2% of the switching period.

TABLE I
Performance Summary and Comparison with the State-of-the-Art

	This work	[6] TPEL '22	[12] STMP30	[13] MAX18000
Technology	**180-nm**	180-nm	180-nm	N/A
V_{in} [V]	**2.5 - 4.8**	2.5 - 4.8	2.5 - 4.8	2 - 4.8
V_{out} [V]	**5**	5	5	5
$I_{load,max}$ [mA]	**600**	800	550	1000
L[μH]	**2.2**	2.2	2.2	0.47
C [μF]	**44**	44	44	44
f_{sw} [MHz]	**1.5**	1.5	1.5	2
η_{peak} [%]	**96.1**	96	96.5	95*
Ctrl method	**VM F-PID**	ICF	CM	N/A
Ctrl Area [mm^2]	**0.23**	0.29	0.3	N/A
ΔI_{load} [mA]	**300**	300	300	985
$\Delta V_{out,pp}$ [mV]	**80**	80	140	200*
ΔV_{in} [V]	**1**	1	1	0.7
$\Delta V_{out,pp}$ [mV]	**40**	87	36	80

*estimated from figure.

References

[1] M. K. Barwar, L. K. Sahu, P. R. Tripathi, P. Bhatnagar, K. K. Gupta, A. H. Chander, and J. M. Guerrero, "Demystifying the devices behind the led light: Led driver circuits," *IEEE Industrial Electronics Magazine*, volume 17, number 1, pages 55–66, 2023.

[2] F. Mao, Y. Lu, E. Bonizzoni, F. Boera, M. Huang, F. Maloberti, and R. P. Martins, "A hybrid single-inductor bipolar-output dc–dc converter with floating negative output for amoled displays," *IEEE Journal of Solid-State Circuits*, volume 56, number 9, pages 2760–2769, 2021.

[3] R. W. Erickson and D. Maksimovic, *Fundamentals of power electronics*. Springer Science & Business Media, 2007.

[4] S. J. Kim, Q. Khan, M. Talegaonkar, A. Elshazly, A. Rao, N. Griesert, G. Winter, W. McIntyre, and P. K. Hanumolu, "High frequency buck converter design using time-based control techniques," *IEEE J. of Solid-State Circuits*, volume 50, number 4, pages 990–1001, 2014.

[5] J.-G. Kang, J. Park, M.-G. Jeong, and C. Yoo, "A time-domain-controlled current-mode buck converter with wide output voltage range," *IEEE J. of Solid-State Circuits*, volume 54, number 3, pages 865–873, 2019.

[6] M. Leoncini, A. Dago, A. Bertolini, A. Gasparini, S. Levantino, and M. Ghioni, "A compact high-efficiency boost converter with time-based control, rhp zero-elimination, and tracking error compensation," *IEEE Trans. on Power Electronics*, volume 38, number 3, pages 3100–3113, 2023.

[7] P. Melillo, S. Zaffin, M. Leoncini, A. Brunero, A. Gasparini, S. Levantino, and M. Ghioni, "A wide-input-range time-based buck converter with adaptive gain and continuous phase preset for seamless pfm/pwm transitions," *IEEE Transactions on Circuits and Systems I: Regular Papers*, pages 1–12, 2024.

[8] M.-L. Chiu, I.-F. Lo, and T.-H. Lin, "A time-domain current-mode buck converter with a pi compensator incorporating an infinite phase shift delay line," *IEEE J. of Solid-State Circuits*, volume 60, number 6, pages 2206–2214, 2025.

[9] N. J. Dahl, P. L. Muntal, and M. A. E. Andersen, "Fully time-based pid controller for a high frequency buck converter," in *2023 21st IEEE Interregional NEWCAS Conference (NEWCAS)*, 2023, pages 1–5.

[10] B. Arbetter and D. Maksimovic, "Feedforward pulse width modulators for switching power converters," *IEEE Transactions on Power Electronics*, volume 12, number 2, pages 361–368, 1997.

[11] M. Kazimierczuk and D. Czarkowski, "Application of the principle of energy conservation to modeling the pwm converters," in *Proc. of IEEE Int. Conference on Control and Applications*, 1993, 291–296 vol.1.

[12] STMicroelectronics, *3-channel pmic for mobile amoled display*, [Rev 1 - Feb. 2022]. [Online]. Available: https://www.st.com/en/power-management/stmp30.html.

[13] *500mv to 5.5v input nanopower boost converter with short-circuit protection*, MAX18000, Rev 0; Analog Devices, Feb. 2023. [Online]. Available: https://www.analog.com/media/en/technical-documentation/data-sheets/max18000.pdf.